Applied Computer Science, vol. 18, no. 1, pp. 5–19
doi: 10.35784/acs-2022-1

Submitted: 2022-02-10 | Revised: 2022-03-14 | Accepted: 2022-03-21

Keywords: FEM, composite spar, main rotor blade, carbon fiber, strength analysis

Rafał KLIZA [0000-0002-7571-158]*, *Karol ŚCISŁOWSKI* [0000-0003-0337-5863]*, *Ksenia SIADKOWSKA* [0000-0002-3315-2102]*, *Jacek PADYJASEK**, *Mirosław WENDEKER* [0000-0003-4121-8818]*

STRENGTH ANALYSIS OF A PROTOTYPE COMPOSITE HELICOPTER ROTOR BLADE SPAR

Abstract

This paper investigates the strenght of a conceptual main rotor blade dedicated to an unmanned helicopter. The blade is made of smart materials in order to optimize the efficiency of the aircraft by increasing its aerodynamic performance. This purpose was achieved by performing a series of strength calculations for the blade of a prototype main rotor used in an unmanned helicopter. The calculations were done with the Finite Element Method (FEM) and software like CAE (Computer-Aided Engineering) which uses advanced techniques of computer modeling of load in composite structures. Our analysis included CAD (Computer-Aided Design) modeling the rotor blade, importing the solid model into the CAE software, defining the simulation boundary conditions and performing strength calculations of the blade spar for selected materials used in aviation, i.e. fiberglass and carbon fiber laminate. This paper presents the results and analysis of the numerical calculations.

1. INTRODUCTION

Composite materials have been recently more and more often applied to aircraft constructions. Constructions of both newly manufactured airplanes and helicopters show a growing share of composite materials. It is worth noting that composite elements are used not only in fuselages but also blades of main rotors. This entails complex loads carried by such a composite material in a main blade. Advanced analytical calculations and numerical simulations become indispensable to correctly design such a blade. Increased interest, especially in 2021, in simulations to design composite blades for helicopter rotor blades was also noticed, which is proven by the publications in the ScienceDirect.com database registered over the last 21 years. The number of publications selected by the keywords of "helicopter composite rotor blade" are listed in Fig. 1.

* Lublin University of Technology, Faculty of Mechanical Engineering, Department od Thermodynamics, Fluid Mechanics and Aviation Propulsion Systems, Lublin, Poland, r.kliza@pollub.pl, k.scislowski@pollub.pl, k.siadkowska@pollub.pl, m.wendeker@pollub.pl

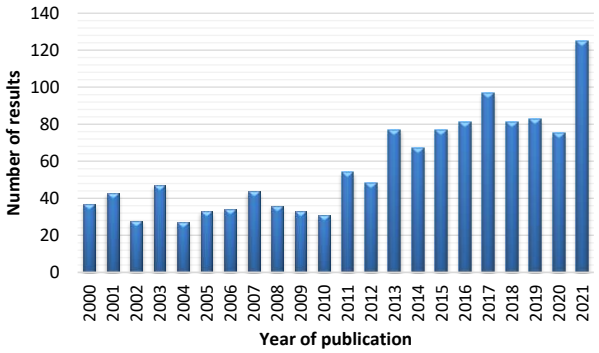

Fig. 1. Number of publications on helicopter composite rotor blade

Airfoils are usually made of thin metal skin plating that is constructed to withstand tensile and compressive loads. The nature of such a structure makes it vulnerable to the process of buckling even under low compressive load. Aerospace structures are reinforced by stiffening a load-bearing airfoil with spars which are a main load-bearing element of a rotor blade. A spar is usually a beam which carries loads that are both concentrated and distributed along the blade. Ribs are mounted to a spar later and such a rotor blade supporting structure prevents deforming the support airfoil. Ribs of the airfoil supporting structure transfer loads from the skin to the spar itself (Megson, 2010). The basic feature of a single-spar wing is that only one main spar is along the entire wing, and ribs and baffles make it aerodynamic. A single-spar construction is rarely used in main rotor blades. A very popular method for constructing main rotor blade support structures is honeycomb. The attempts to improve honeycomb structures of rotor blades by increasing strength and stiffness of the entire structure are discussed in several papers (Peng & Bargmann, 2021; Teter & Gawryluk, 2016; Jaafar, Makich & Nouari, 2021; Sukmaji et al., 2017). One way to improve the design of the blade support structure is to make the shape of the structure itself more optimized, which means that, e.g. structures of main rotors are less loaded but their aerodynamic and strength properties remain similar. Defects and methods of their detection in honeycomb structures in plastic rotor blades are classified in several papers (Balaskó et al., 2005; Shahani & Mohammadi, 2015; Rathod, Tiwari & Chougale, 2019; Klochkov et al., 2021). Attention has also been paid to identify typical defects during production of honeycomb blades.

With the increasing popularity of plastics in general industry, the aerospace industry has also become interested in manufacturing such aircraft components. Particular attention has been given to use composites for aerospace applications which account for approximately 70% of the cost of aircraft components. An increasing number of airframe components are being made from non-metallic materials, and one of them is the main rotor spar made more and more frequently of polymer composites. Its greatest advantage is that the weight of such a component is approximately half that of metal alloys, its fatigue strength remains the same and such components can be connected without screws and rivets. Reducing the weight of polymer composite elements is possible due to the low density of materials used in the production of the composite. High strength is achieved by using fiber matrices with high stiffness and strength in the direction of fiber alignment. No screw and rivet connections are possible due to the adhesive properties of composites. The bonding process can occur between two metals, metal and composite, and between two composites (Waghmare et al.,

2021; Kang et al., 2021; Li et al., 2021). An example is bonding the rotor blade skin to ribs and spars inside the blade. Polymer composites used in aviation take one of two forms. The first form is a composite in the form of a laminate where each layer has a different angle of arrangement of fibers, which results in uniform strength in each direction. The second form is a composite of the so-called "sandwich" structure. This structure has a core in its center to provide stiffness to the structure and its outer layers are made of laminate to increase the ability to transfer longitudinal loads (Grodzki, Łukasiewicz & Leśniewska, 2015; Puchała, Jachimowicz & Szymczyk, 2014). The core is bonded to the outer laminate through the so-called adhesive layer. In sandwich composites, the core plays a key role and must provide sufficient stiffness. The effect of core-dependent stabilization of the entire composite is presented in the research paper (Michalski & Krauze, 2019) that focuses on honeycomb cores.

Tab. 1. Properties of the most common polimer composites

Parameter	Carbon fibers (50% of volume)	Glass fibers (50% of volume)	Kevlar fibers (type 49)	Graphite fibers (T300/5208)
Density [kg/m^3]	1800	2.6	1.4	1.8
Young Modulus [GPa]	230	76	112.4	132
Tensile strenght [GPa]	4.2	3.5	3.0	5.7
Extension (%)	1.9	4.8	2.4	2.8

At present, research is being conducted all the time to improve safety, manufacturing, efficiency, and optimization of polymeric structures. The research paper (Visweswaraiah et al., 2013) focuses on optimization depending on the layer angle and internal geometry of composite materials in a helicopter blade. The publication (Taymaz, 2017) provides information on optimization of composite joints by using innovative algorithms in CAE type programs. Research is also conducted to improve the reliability of composite materials as in the article (Rasuo, 2011) where modern experimental techniques are studied to evaluate the fatigue characteristics of laminated structures. In addition, the publication (Szymański, 2020) presents certain ways of the non-destructive testing of thermoplastic composites made of carbon fibers. The main aspect of the influence of hole preparation in composites on their properties is, in turn, presented in (Karny, 2017).

This paper discusses the strength calculations of a prototype main rotor blade spar used in an unmanned helicopter. The calculations were performed with the Finite Element Method and Computer-Aided Engineering software. The strength calculations were performed for the blade spar made of selected materials that are used in aviation.

2. MATERIALS AND METHOD

2.1. Preparing of the rotor blade spar model

The spar was simulated as a static case in ABAQUS. The first calculation step was reduced by the given options to make a more accurate analysis, increase the maximum calculation steps and the minimum increment of the calculation progress. The force application points and the model restraints were determined after the material data were entered to create the 3D model. The support points of the 3D model were determined by

specifying points, lines or planes where the support were be located. Next, the degrees of freedom to be received at the determined locations were selected. The forces acting on the test object were specified just like the support locations were selected, but the type of force acting at a given location was also selected. The type of correlations enables us to modify, e.g. characteristics of friction coefficient between objects or stiffening many parts for a single element. Finally, prior to calculations a model is discretized, which means dividing an object into smaller sections called finite elements. This process requires us to select a correct finite element mesh to show a geometric shape, number of nodes, function of this shape or size of each element. A particularly important parameter is the size of a single finite element. Simulation time becomes longer due to improving accuracy and reducing the size of such an element by maintaining the shape of the test object (Wysmulski, Debski & Falkowicz, 2020; Debski, Rozylo & Wysmulski, 2020; Azad, Mirghaderi & Epackachi, 2021, Różyło & Wrzesińska, 2016). Main rotor simulations in CAE computer programs are typically strength simulations. Numerical calculations are mainly to analyze the deflection of rotor spars and adjacent parts as well as values of maximum stresses at the connection points with other elements. Practical application of the FEM simulation method to obtain preliminary data about the strength of spars with actuators for changing the angle of the entire blade is discussed in the paper (Siadkowska & Borowiec, 2021). In another paper, the simulation was carried out to verify the strength of the model under a given load resulting from flight conditions (Skiba, 2019). The possibility of testing different solutions in the design of holes in the main shaft of the main rotor and the effect of the chosen solution on the maximum stress under a given load was also presented (Skiba et al., 2021). The tested object was a three-dimensional model of the spar, shown below, which was designed using CATIA V5 R21.

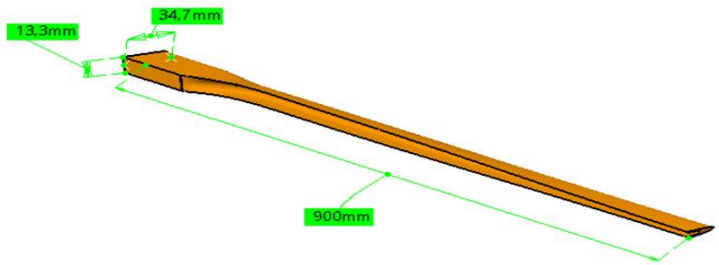

Fig. 2. Spar model with its overall dimensions generated in CATIA V5 R21

The model shows a spar that can be used in a prototype unmanned helicopter with a maximum mass of up to 150 kg. Ultimately, the smart materials technology is also planned to improve aerodynamic efficiency during each phase of flight. Better aerodynamics was possible by changing the geometry of the main rotor blades so it was decided to perform strength simulations of the spar that is the supporting element of this blade. For this project, a configuration of eight layers of composite was selected and two simulations with a fiber distribution of 0/45/-45/90S and 0/90 were carried out. For clarity, in Tab. 2, abbreviated symbols have been assigned to the individual composite configurations to ease further interpretation of the numerical simulation results.

Tab. 2. Summary of the composite configurations used for numerical analyses

Composite fibre type	Arrangement configuration	Short name
Carbon fiber	0/45/-45/90S	Model 1
Carbon fiber	0/90S	Model 2
Glass fiber	0/45/-45/90S	Model 3
Glass fiber	0/90S	Model 4

The fiber distribution was chiefly parallel to the longitudinal axis of the spar. Unlike isotropic materials, it was required to specify in composites material data for different load directions. The material data determined for the simulations are shown in Tab. 3 both for the carbon fiber composite and the glass fiber composite.

Tab. 3. Material data with units for carbonfiber/epoxy and fiberglass/epoxy resin composites

Parameter	Carbonfiber	Fiberglass
Density δ	1800 kg/m^3	2600 kg/m^3
Young modulus in paralel direction to fiber arragement E_1	$2.3 \cdot 10^5$ MPa	$7.6 \cdot 10^4$ MPa
Young modulus in perpendicular direction to fiber arragement E_2	$7.5 \cdot 10^3$ MPa	$1.59 \cdot 10^4$ MPa
Poisson ratio in the ν fiber plane	0.31	0.25
Kirchhoff modulus G12 in the XY plane	4 510 MPa	5 810 MPa
Kirchhoff modulus G13 in the XZ plane	4 510 MPa	5 810 MPa
Kirchhoff modulus G23 in the YZ plane	3 050 MPa	5 690 MPa
Material type	Laminate	Laminate

The fiber arrangement is illustrated in Fig. 3 for model 1 and 3. Each of the eight layers occupies 12.5% of the laminate volume. All layers have the same thickness.

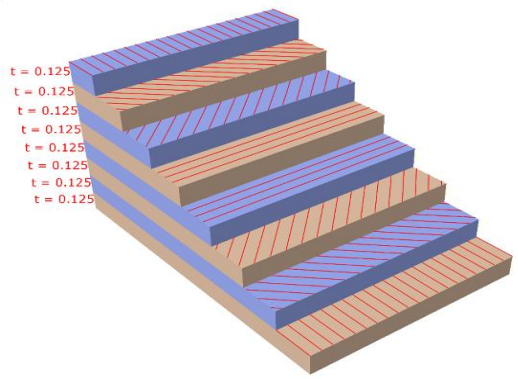

Fig. 3. Fiber alignment for model 1 and 3

A three dimensional tetrahedral mesh was superimposed on the model. This computational mesh consisted of 12 654 elements and 18 370 nodes. The number of elements and the exact type of the finite element mesh is large enough to claim that the simulation calculations are valid and a computation time is short.

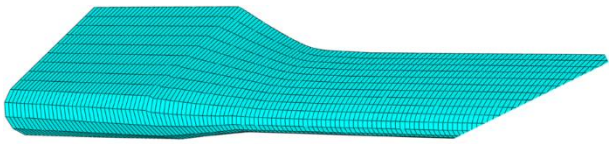

Fig. 4. A spar as a discrete element

2.2. CAE numerical program

The spar was simulated as a static case using the "Static, General" option in ABAQUS. The loads were defined by introducing boundary conditions in the form of fixing the spar at its cap. Movement along X, Y and Z axes was blocked but rotation was possible around the X axis. Next, the forces acting on spar were defined. The first one was the gravitational force as the "gravity" type in units of m^2/s being opposite to the Y axis. The force referred to the whole model and its value was distributed uniformly. The centrifugal force to simulate the rotational motion of the spar during flight acts on the axis of the points of [0;0;0] and [0;1;0], i.e. around the Y axis. The centrifugal force was modeled by the function of "Rotational body force" with a centrifugal force effect, and speed was set up as 1200 rpm, or 125.66 rad/s. This force acted uniformly on the entire model. Another component was the lift force generated during the flight of the machine. The induced losses at the blade tip were neglected in the analysis. The lift force acted along the Y axis increasing from the blade cap to its tip. Its value was 500 N, starting from 125 N where the load distribution began. The load distribution was along 750 mm. The load function creation option in ABAQUS was used to simulate this force. Similarly, a drag force estimated as 30 N was introduced starting from 7.6 N where the force originated. The final step was to introduce the spar torsional moment by setting a concentrated moment at the end of the spar of 15 Nm. The torsional moment was distributed uniformly to the plane at the end. A centrifugal force was applied to the blade during the simulated operating conditions, the value of which is calculated from equation (1):

$$F_C = m * \omega^2 * R \tag{1}$$

where: m – mass,
ω – angular velocity,
R – blade length.

The tensile stresses are therefore calculated from the formula:

$$\sigma_b = \frac{F_c}{A} \tag{2}$$

where: F_c – tensile force,
A – cross section of the spar.

In addition to the tension due to the centrifugal force, the spar also carries bending stresses due to the lift force and the drag force. To determine this, start by determining the bending moment from the lifting force in the following formula (3):

$$\sigma_x = \frac{M_{bx}}{W_x} \tag{3}$$

where: M_{bx} – bending moment against the X axis,
W_x – bending strength index also against the X axis.

The bending moment is calculated from the resultant force causing bending and the arm on which it acts relative to where the blade is attached. The resultant force is calculated from the given linear load distribution (4):

$$F_{Lt} = \frac{(F_{Lmax} - F_{Lmin}) * L}{2} + F_{Lmin} * L \tag{4}$$

where: F_{Lt} – resultant of the lift vector,
F_{Lmin} – minimum lift assumed to be 125 N,
F_{Lmax} – maximum lift assumed to be 500 N,
L – distance over which the lift acts is 750 mm.

The section over which the force acts is determined by the following formula:

$$L_t = \frac{\left(F_{Lmin} * \frac{L}{2}\right) + \left[(F_{Lmax} - F_{Lmin}) * \frac{2}{3} * L\right]}{F_{Lt}} \tag{5}$$

which after substituting the formula for the value of F_{Lt} gives formula (6).

$$L_t = \frac{\left(F_{Lmin} * \frac{L}{2}\right) + \left[(F_{Lmax} - F_{Lmin}) * \frac{2}{3} * L\right]}{\frac{(F_{Lmax} - F_{Lmin}) * L}{2} + F_{Lmin} * L} \tag{6}$$

Therefore, the bending moment formula can be written as in (7).

$$M_{bx} = F_{Lt} * L_t = \left[\frac{(F_{Lmax} - F_{Lmin}) * L}{2}\right] + (F_{Lmin} * L) * \left\{\frac{\left(F_{Lmin} * \frac{L}{2}\right) + \left[(F_{Lmax} - F_{Lmin}) * \frac{2}{3} * L\right]}{\frac{(F_{Lmax} - F_{Lmin}) * L}{2} + F_{Lmin} * L}\right\} \tag{7}$$

To determine bending stresses, it is necessary to calculate the bending strength ratio with respect to the X axis. Equation (8) defines this ratio as:

$$W_x = \frac{J_x}{e_{max}} \tag{8}$$

where: J_x – geometric moment of inertia against the bending neutral axis,
e_{max} – distance from the bending neutral axis to the outermost point of the cross-sectional contour of the spar.

Thus, the bending stresses from the lifting force will be expressed by equation (9).

$$\sigma_{bx} = \frac{\left[\frac{(F_{Lmax} - F_{Lmin}) * L}{2} + F_{Lmin} * L\right] * \left\{\frac{\left(F_{Lmin} * \frac{L}{2}\right) + \left[(F_{Lmax} - F_{Lmin}) * \frac{2}{3} * L\right]}{\frac{(F_{Lmax} - F_{Lmin}) * L}{2} + F_{Lmin} * L}\right\}}{\frac{J_x}{e_{max}}} \quad (9)$$

Exactly the same formulas apply to blade bending by frictional forces. The difference is the plane of action of the forces so the reference point for the bending formulae is the Y axis.

Hence, to calculate the total bending stress with respect to the X and Y axes, it is necessary to apply formula (10):

$$\sigma_b = \sqrt{{\sigma_{bx}}^2 + {\sigma_{by}}^2} \quad (10)$$

where: σ_b – total bending stress,
σ_{bx} – bending stress against the X axis,
σ_{by} – bending stress against the Y axis.

Since the blade is also twisted, the total stresses from the force moments are calculated using the Huber hypothesis formula (11):

$$\sigma_{overall} = \sqrt{{\sigma_b}^2 + 3{\tau_t}^2} \quad (11)$$

where: $\sigma_{overall}$ – total stress value,
σ_b – normal stress from bending moments,
τ_t – tangential stress from torsional moments.

3. SIMULATION RESULTS AND DISCUSION

3.1. Composite spar simulation results for model 1

During strength analysis of composites, a key aspect is to determine fiber alignment and stresses acting in each layer. For this reason, loads in two stress states: stresses along the main axis of fiber arrangement (Fig. 5a) and stresses transverse to the main axis of fiber alignment (Fig. 5b) were analyzed in the composite models under consideration. The maximum stress reaches 591 MPa. In the case of stress distribution perpendicular to the main axis of fiber alignment (Fig. 5b), the stresses transmitted through the material are much smaller and reach the highest value of 17 MPa. The strength of carbon fibers perpendicular to the main axis of fiber alignment is estimated to be about 900 MPa, so the material should retain its strength properties at maximum stresses. The deformations along the X-axis (Fig. 6a) reach a maximum displacement of 4 mm opposite to the X-axis. The displacements along in the Y-axis (Fig. 6b) reach a maximum value of 85 mm at the end of the spar.

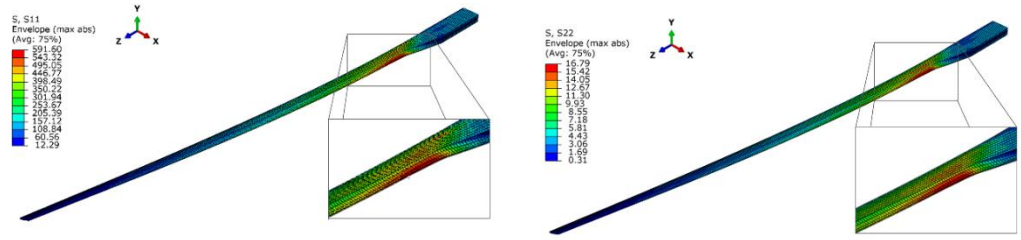

a) **b)**

Fig. 5. Overall stresses for carbon fiber/epoxy resin composite: a) along the main axis of fiber alignment, b) perpendicular to the main axis of fiber alignment.

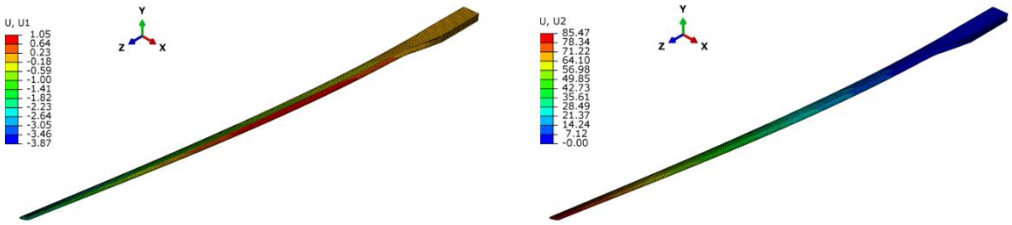

a) **b)**

Fig. 6. Deformations in carbon fiber composite spar: a) along the X-axis, b) along the Y-axis

The maximum stresses that occurred are longitudinal to the fiber alignment. Due to the laminate structure, the individual stresses in the fibers that occurred in each alignment variant of model 1 were analyzed later in this article (Fig. 7, Fig. 8). The fibers aligned along the main alignment axis show stresses in the range of -458 MPa ÷ 538 MPa. The laminate layer with the fibres aligned at 45° shows lower stresses with the maximum value of 262 MPa for fibre tension and 152 MPa for fibre compression (Fig. 7b). The stresses in the -45° laminate layer (Fig. 8a) show differences in stresses with respect to the +45° laminate, i.e. the highest stresses reached 187 MPa for tension and 205 MPa for compression.

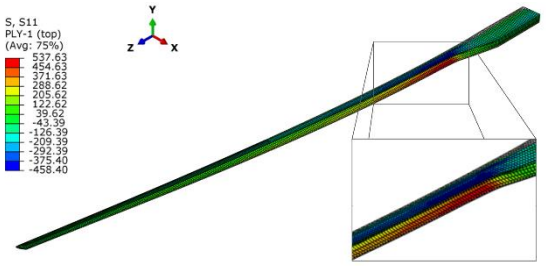

Fig. 7. Stresses in the fiber layer along the main axis of fiber alignment

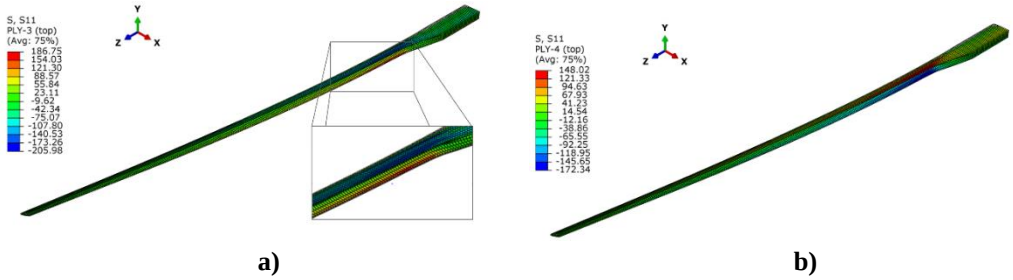

a) **b)**

Fig. 8. Stresses in the layer with fibers: a) angled (-45°) to the main axis of fiber alignment, b) perpendicular (90°) to the main axis of fiber alignment

The last layer analyzed was the layer with fibers aligned at the angle of 90° (Fig. 8b). The maximum stresses were 148 MPa for tension and 172 MPa for compression. A significant change compared to the case in Fig. 6 is that compression occurs at the cap of the spar and tension at the tip. The analysis of the results from each separate laminate layer shows that the highest stresses occurred in the layer with fibres parallel to the longitudinal axis of the spar because of the alignment of the fibers taking up the largest portion of the bending stresses that occurred when the load-bearing force was generated in the spar. For the fibers transverse to the first layer, the stresses were much lower and compression and tension occurred on the opposite sides of the spar. This may be due to the greater transfer of load caused by the drag force and the bending moment in the fibers transverse to the longitudinal axis of the spar and a negligible transfer of the bending moment caused by the lifting force.

3.2. Composite spar simulation results for model 2

The next variant was a spar made of carbon fiber with epoxy resin, with layers aligned alternately at 0° and 90°. The maximum stresses along the main axis of fiber alignment reached 504 MPa (Fig. 9). The highest stresses occurred on both the bottom and top surfaces. The maximum stresses were by 87 MPa (14%) lower than those in the composite with a uniform fiber alignment. As in the model 1, transverse stresses were significantly lower than longitudinal ones with a maximum value of 15 MPa near the spar cap. This is a difference of 2 MPa compared to the composite with parallel fibers. The model displacements of along in the X axis (Fig. 10a) were more than those of the 0/45/-45/90 composite and the maximum deformation was 8 mm at the spar tip. On the other hand, the displacements along the Y axis (Fig. 10b) were smaller, i.e. 77 mm compared to 85 mm in the composite with fibers arranged uniformly at each angle.

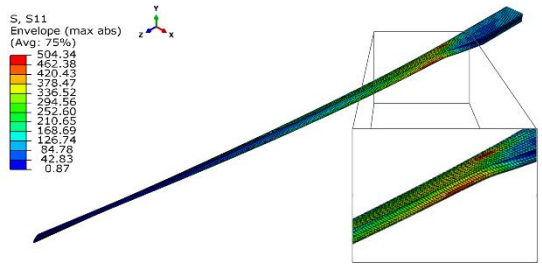

Fig. 9. General stresses along the main axis of fiber alignment

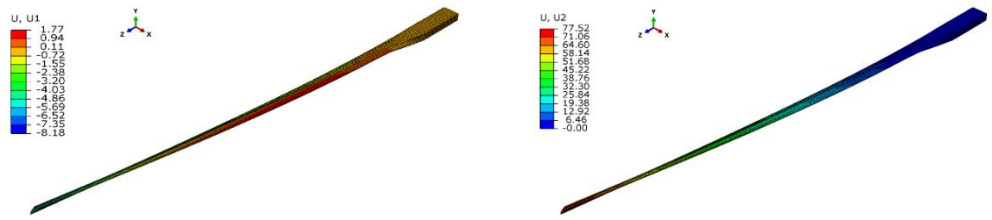

a) **b)**

Fig. 10. Deformations in the carbon fiber composite spar: a) along the X axis, b) along the Y axis

Each layer with fibers aligned at 0° had a similar stress distribution. The maximum values changed, depending on the position of the layer in the composite. Fig. 11 shows the stress distribution for each layer. Tab. 4 shows the individual values of stresses. The first layer is closest to the inner part of the spar, while the eight layer is closer to the outer surface. The stresses in the layers with fibers at the angle of 90° are presented in a similar manner. Tab. 5 shows the stress values in each layer. The simulation shows that the fibers arranged along the spar carry 5 times higher loads than the fibers arranged transversely to the spar because of better properties of transferring the bending load of the spar by the generated load force along its length.

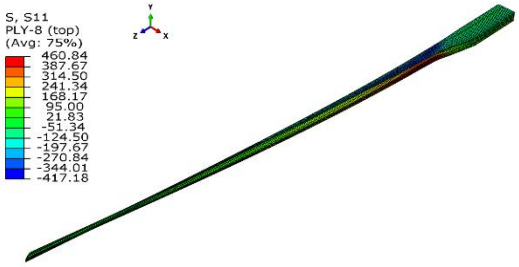

Fig. 11. Stresses in the fiber layer along the main axis of fiber alignment.

Tab. 4. Stress values for the layers with fibers aligned at 0°

Layer	Tensile stresses [MPa]	Compressive stresses [MPa]
First	400	383
Third	416	392
Sixth	439	404
Eight	455	414

Tab. 5. Stress values for the layers with fibers aligned at 90°

Layer	Tensile stresses [MPa]	Compressive stresses [MPa]
Second	55	87
Fourth	34	34
Fifth	35	37
Seventh	79	49

3.3. Composite spar simulation results for model 3

A simulation was performed for a composite made of fiberglass and epoxy resin. Fig. 12 shows the overall stresses for the variant according to model 3 and its maximum stress was 252 MPa, which is much lower than in the case of the carbon fiber spar with the same fibers alignment (591 MPa). The stresses transverse to the fiber alignment reached 48 MPa, which is by 31 MPa higher than in the carbon fiber composite with the same fiber alignment.

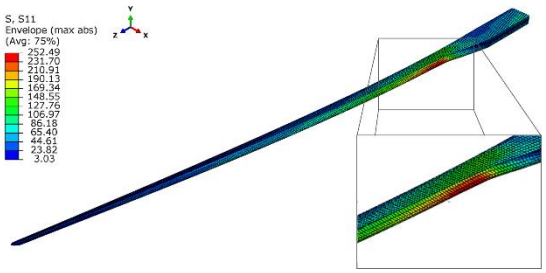

Fig. 12. General stresses along the main axis of fiber alignment

The fibers aligned along the main axis showed stresses of 250 MPa for tension and 144 MPa for compression (Fig. 13). The distribution of stresses was similar to their overall distribution in the spar. For the layer with fibers at 45°, the stresses decreased and were 124 MPa for tension and 42 MPa for compression. The layer with fibers at -45° showed even lower stresses reaching 86 MPa for tension and 65 MPa for compression of the fibers. The last layer had fibers arranged at 90°, and the stresses here were the lowest of all layers. The tensile stress of the fibers was 47 MPa and the compressive stress was 66 MPa. The fiber compression in this layer occurred at the tip of the spar, and the tension at its cap which is opposite to the other layers.

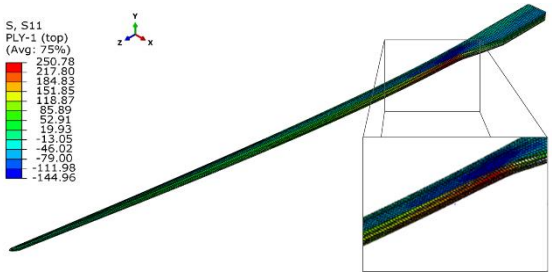

Fig. 13. Stresses in the layer with fibers along the main axis of fiber alignment (0°)

3.4. Composite spar simulation results for model 4

The last variant was a model 4 composite spar. The maximum stresses along the main axis of fiber alignment reached 232 MPa. Fig. 14 shows the stress distribution in the spar. The maximum transverse stresses were 47 MPa, which is 5 times lower than the longitudinal stresses. In the case of separate layers, each layer with a fiber alignment angle of 0° had a similar stress distribution. The maximum values changed, depending on the position of the layer in the composite. Fig. 15a shows the stress distribution for the layer with a 0° fiber alignment angle, while Tab. 6 shows the values in the individual layers. The stresses in each of the layers with a 90° fiber alignment angle are described in a similar manner. Fig. 15b shows the stress distribution in these layers, and Tab. 7 shows their values.

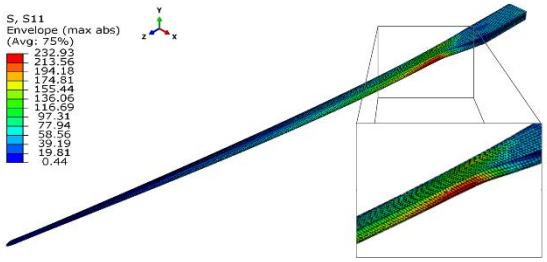

Fig. 14. General stresses along of the main axis of fiber arrangement

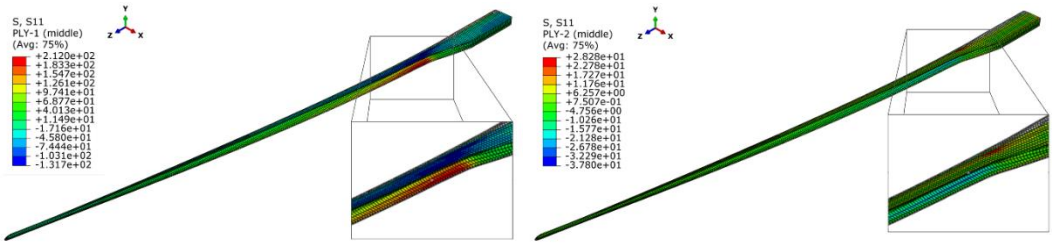

a) **b)**

Fig. 15. Stresses in a layer with fibers: a) along the main axis of fiber alignment (0°), b) perpendicular to the main axis of fiber alignment (90°)

Tab. 6. Stress for the layers with a 0° angle of fiber alignment

Layer	Tensile stress [MPa]	Compressive stress [MPa]
First	212	131
Third	217	135
Sixth	226	140
Eight	231	144

Tab. 7. Stress for the layers with a 90° angle of fiber alignment

Layer	Tensile stress [MPa]	Compressive stress [MPa]
Second	28	37
Fourth	25	25
Fifth	24	24
Seventh	27	26

4. CONCLUSIONS

This paper discusses the strength simulation of the spar support rotor of an unmanned helicopter. The research scope included a preparation of a 3D model for ABAQUS software analysis and a strength simulation based on theoretical forces acting on the spar during flight. The selected composite materials were simulated for four fiber alignment variants. The results on displacement and stress do not uniquely determine the behavior of the given model under real loading due to the idealized nature of FEM strength simulations. The stress in the model 1 carbon fiber composite was by 17% higher than in the model 2 alignment (591 MPa vs. 504 MPa). The transverse stress was identical to that in the glass fiber composite, i.e. 16 MPa and was significantly lower than the tension stress. The carbon composite showed significantly different displacement along the X axis than the glass fiber composite. The displacement in the model 1 was 4 mm and as much as 8 mm in the model 2, which is a double deformation difference. The displacements along the Y axis are more similar with

a difference of only 10%. The differences between the fiberglass spar in the configuration of model 3 and 4 are seen in the maximum stresses. The mentioned stresses differ by 8% and reach 252 MPa for the model 3 composite and 232 MPa for the model 4 composite. The fiber alignment had no significant effect on the spar tension values along the Y axis. The tension difference was 4%: the displacements along the X axis were not higher than 14%. The stresses transverse to the spar in each composite fiber alignment variant were significantly smaller than the stresses along the composite. This means that most of the stresses originated from the spar bending induced by the lifting force. The lowest transverse stresses, i.e. 16 MPa were recorded for the carbon fiber composite and the highest, i.e. 48 MPa for the glass fiber composite.

The obtained results enabled the preliminary determination of the rotor blade spar loads for selected fiber arrangement configurations and fiber type. The conclusion drawned from the numerical results is that the values less than the maximum allowable load were achieved for each fiber alignment configuration. The research results show that the most favorable solution is to the model 1. Carbon fibre shows uniform strength in each direction and low loads relative to its ultimate strength. Despite the high excess strength of the spar, its use over many years can lead to fatigue and lower ultimate load values so the model 2 and model 4 variants may be less effective.

Acknowledgments

This work has been financed by the National Center for Research and Development under the LIDER IX program. Grant Agreement No. LIDER/45/0177/L-9/17/NCBR/2018.

Conflicts of Interest

The authors declare that they have no known competing financial interests or personal realtionships that could have appeared to influence the work reported in this paper.

REFERENCES

Azad, S., Mirghaderi, S. R., & Epackachi, S. (2021). Numerical investigation of steel and composite beam-to-encased composite column connection via a through-plate. *Structures*, *31*(December 2020), 14–28. https://doi.org/10.1016/j.istruc.2021.01.040

Balaskó, M., Sváb, E., Molnár, G., & Veres, I. (2005). Classification of defects in honeycomb composite structure of helicopter rotor blades. *Nuclear Instruments and Methods in Physics Research, Section A: Accelerators, Spectrometers, Detectors and Associated Equipment*, *542*(1–3), 45–51. https://doi.org/10.1016/j.nima.2005.01.010

Debski, H., Rozylo, P., & Wysmulski, P. (2020). Stability and load-carrying capacity of short open-section composite columns under eccentric compression loading. *Composite Structures*, *252*, 112716. https://doi.org/10.1016/j.compstruct.2020.112716

Grodzki, W., Łukasiewicz, A., & Leśniewska, K. (2015). Modelling of UAV'S Composite Structures and Prediction of Safety Factor. *Applied Computer Science*, *11*(3), 67–75.

Jaafar, M., Makich, H., & Nouari, M. (2021). A new criterion to evaluate the machined surface quality of the Nomex® honeycomb materials. *Journal of Manufacturing Processes*, *69*, 567–582. https://doi.org/10.1016/j.jmapro.2021.07.062

Kang, Z., Shi, Z., Lei, Y., Xie, Q., & Zhang, J. (2021). Effect of the surface morphology on the bonding performance of metal/composite hybrid structures. *International Journal of Adhesion and Adhesives*, *111*, 102944. https://doi.org/10.1016/j.ijadhadh.2021.102944

Karny, M. (2017). The influence of the fastener hole preparation method on the fastener pull-through process in a carbon composite. *Transactions on Aerospace Research*, *1*(246), 45–53. https://doi.org/10.2478/tar-2017-0005

Klochkov, N., Zverkov, I., Kurlaev, N., & Ahmed, M. S. (2021). Improvement of non-destructive testing methods in diagnostics of composite honeycomb structures of civil aircraft. *AIP Conference Proceedings*, *2402*, 020045. https://doi.org/10.1063/5.0071712

Li, X., Wang, B., Xu, D., Wang, B., Dong, W., & Li, M. (2021). Super-high bonding strength of polyphenylene sulfide-aluminum alloy composite structure achieved by facile molding methods. *Composites Part B: Engineering*, *224*, 109204. https://doi.org/10.1016/j.compositesb.2021.109204

Megson, T. H. G. (2010). Introduction to Aircraft Structural Analysis. In *Introduction to Aircraft Structural Analysis*. Elsevier. https://doi.org/10.1016/C2009-0-62169-3

Michalski, M., & Krauze, W. (2019). Influence of honeycomb core stabilization on composite sandwich structure geometry. *Transactions on Aerospace Research*, *3*(256), 1–13. https://doi.org/10.2478/tar-2019-0013

Peng, X. L., & Bargmann, S. (2021). A novel hybrid-honeycomb structure: Enhanced stiffness, tunable auxeticity and negative thermal expansion. *International Journal of Mechanical Sciences*, *190*, 106021. https://doi.org/10.1016/j.ijmecsci.2020.106021

Puchała, K., Jachimowicz, J., & Szymczyk, E. (2014). Analysis of load transfer into composite structure. *Applied Computer Science*, *10*, 86–94.

Rasuo, B. (2011). Experimental Techniques for Evaluation of Fatigue Characteristics of Laminated Constructions from Composite Materials: Full-Scale Testing of the Helicopter Rotor Blades. *Journal of Testing and Evaluation*, *39*(2), 237–242. https://doi.org/10.1520/JTE102768

Rathod, S., Tiwari, G., & Chougale, D. (2019). Ballistic performance of ceramic-metal composite structures. *Materials Today: Proceedings*, *41*, 1125–1129. https://doi.org/10.1016/j.matpr.2020.08.759

Różyło, P., & Wrzesińska, K. (2016). Numerical Analysis of Buckling and Critical Forces in a Closed Section Composite Profile. *Applied Computer Science*, *12*(2), 54–62.

Shahani, A. R., & Mohammadi, S. (2015). Damage tolerance approach for analyzing a helicopter main rotor blade. *Engineering Failure Analysis*, *57*, 56–71. https://doi.org/10.1016/j.engfailanal.2015.07.025

Siadkowska, K., & Borowiec, P. (2021). Strength analysis of the conceptual model of a main rotor blade spar with actuators. *Journal of Physics: Conference Series*, *1736*(1), 012021. https://doi.org/10.1088/1742-6596/1736/1/012021

Skiba, K. (2019). Designing and FEM simulation of the helicopter rotor and hub. *IOP Conference Series: Materials Science and Engineering*, *710*, 012003. https://doi.org/10.1088/1757-899X/710/1/012003

Skiba, K., Raczynski, R., Kliza, R., & Wendeker, M. (2021). Strength analysis of a propulsion shaft dedicated for the main rotor test bench. *Journal of Physics: Conference Series*, *1736*(1), 012052. https://doi.org/10.1088/1742-6596/1736/1/012052

Sukmaji, I. C., Wijang, W. R., Andri, S., Bambang, K., & Teguh, T. (2017). Application of sandwich honeycomb carbon/glass fiber-honeycomb composite in the floor component of electric car. *AIP Conference Proceedings*, *1788*, 030056. https://doi.org/10.1063/1.4968309

Szymański, R. (2020). Non-destructive testing of thermoplastic carbon composite structures. *Transactions on Aerospace Research*, *1*(258), 34–52. https://doi.org/10.2478/tar-2020-0003

Taymaz, H. A. (2017). Optimization of Composite Couplings in Helicopter Rotor Blade Spar Using Hybrid Particle Swarm-Gradient Algorithm. *Bilge*, *1*(2), 71–78.

Teter, A., & Gawryluk, J. (2016). Experimental modal analysis of a rotor with active composite blades. *Composite Structures*, *153*, 451–467. https://doi.org/10.1016/j.compstruct.2016.06.013

Visweswaraiah, S. B., Ghiasi, H., Pasini, D., & Lessard, L. (2013). Multi-objective optimization of a composite rotor blade cross-section. *Composite Structures*, *96*, 75–81. https://doi.org/10.1016/j.compstruct.2012.09.031

Waghmare, S., Shelare, S., Aglawe, K., & Khope, P. (2021). Materials Today: Proceedings A mini review on fibre reinforced polymer composites. *Materials Today: Proceedings*, in press. https://doi.org/10.1016/j.matpr.2021.10.379

Wysmulski, P., Debski, H., & Falkowicz, K. (2020). Stability analysis of laminate profiles under eccentric load. *Composite Structures*, *238*, 111944. https://doi.org/10.1016/j.compstruct.2020.111944